JGR Space Physics

RESEARCH ARTICLE
10.1029/2025JA034657

Evidence of an Extended Alfvén Wing System at Enceladus: Cassini's Multi-Instrument Observations

L. Z. Hadid[1], T. Chust[1], J.-E. Wahlund[2], M. W. Morooka[2], E. Roussos[3], O. Witasse[4], J. Rabia[5], D. Pisa[6], K. Kim[2,7], N. J. T. Edberg[2], A. M. Rymer[8], L. Lamy[9,10], S. Kotsiaros[11], S. Aizawa[1], A. Jeandet[1], R. Modolo[12], N. André[5,13], P. Canu[1], C. F. Bowers[14], X. Jia[14], A. J. Coates[15,16], G. H. Jones[4,15], A. Parsec-Wallis[15,16], O. Agiwal[17], M. K. G. Holmberg[18], Q. Nénon[12], H. Cao[19], W. S. Kurth[20], and M. K. Dougherty[21]

[1]Laboratoire de Physique des Plasmas (LPP), CNRS, Observatoire de Paris, Sorbonne Université, Université Paris Saclay, Ecole polytechnique, Institut Polytechnique de Paris, Palaiseau, France, [2]Swedish Institute of Space Physics, Uppsala, Sweden, [3]Max Planck Institute for Solar System Research, Goettingen, Germany, [4]ESTEC, European Space Agency, Noordwijk, The Netherlands, [5]Institut de Recherche en Astrophysique et Planétologie, CNRS-UPS-CNES, Toulouse, France, [6]Department of Space Physics, Institute of Atmospheric Physics of the Czech Academy of Sciences, Prague, Czechia, [7]Department of Physics and Astronomy, Uppsala University, Uppsala, Sweden, [8]Applied Physics Laboratory, John Hopkins University, Laurel, MD, USA, [9]LAM, Aix Marseille Université, CNRS, CNES, Marseille, France, [10]LIRA, Observatoire de Paris, Université PSL, Sorbonne Université, Université Paris Cité, Cergy Paris Université, CNRS, Meudon, France, [11]ESAC, European Space Agency, Madrid, Spain, [12]LATMOS/IPSL - Sorbonne Université, UVSQ, CNRS, CNES, Paris, France, [13]Institut Supérieur de l'Aéronautique et de l'Espace (ISAE-Supaero), Toulouse, France, [14]Department of Climate and Space Sciences and Engineering, University of Michigan, Ann Arbor, MI, USA, [15]Mullard Space Science Laboratory, University College London, Dorking, UK, [16]Centre for Planetary Science at UCL/Birkbeck, London, UK, [17]Boston University, Boston, MA, USA, [18]School of Cosmic Physics, DIAS Dunsink Observatory, Dublin Institute for Advanced Studies, Dublin, Ireland, [19]Department of Earth, Planetary, and Space Sciences, University of California, Los Angeles (UCLA), Los Angeles, CA, USA, [20]Department of Physics and Astronomy, University of Iowa, Iowa City, IA, USA, [21]Physics Department, The Blackett Laboratory, Imperial College London, London, UK

Key Points:

- Enceladus sustains an extended Alfvén wing system with numerous reflections within its torus and on the kronian ionosphere
- Enceladus' electromagnetic interaction with Saturn's rotating magnetic field extends up to at least 120° downstream of the moon
- The large-scale Alfvén wing perturbations are systematically filamented during their propagation at any distance from their source

Supporting Information:

Supporting Information may be found in the online version of this article.

Correspondence to:

L. Z. Hadid,
lina.hadid@lpp.polytechnique.fr

Citation:

Hadid, L. Z., Chust, T., Wahlund, J.-E., Morooka, M. W., Roussos, E., Witasse, O., et al. (2026). Evidence of an extended Alfvén wing system at Enceladus: Cassini's multi-instrument observations. *Journal of Geophysical Research: Space Physics*, *131*, e2025JA034657. https://doi.org/10.1029/2025JA034657

Received 12 SEP 2025
Accepted 18 DEC 2025

Abstract We report in situ evidence for Enceladus' Alfvén wing system and its coupling with Saturn's ionosphere, based on multi-instrument observations from the Cassini spacecraft. Analysis of 36 events, including 13 from non-flyby paths, confirms the existence of a Main Alfvén Wing (MAW) current system generated at Enceladus, and associated Reflected Alfvén Wings (RAWs) occurring both at Saturn's ionosphere and on the density gradient of Enceladus' plasma torus, extending longitudinally to at least ∼120° (∼2,000 moon radii) downstream of the moon. Additionally, the observations reveal the systematic existence of a filamentation process of these large-scale Alfvénic perturbations (MAW and RAWs) during their propagation at any distance from their source. These findings demonstrate a more extensive electrodynamic coupling than previously reported for Enceladus and more generally for any moon-magnetosphere interaction. Moreover, the observation of energetic electron depletions and water-group ion signatures at longitudes even further from the moon supports the interpretation of an extended and persistent interaction region. These results highlight Enceladus' role in shaping Saturn's magnetospheric environment and underscore the importance of future missions to exhaustively analyze this type of complex interaction between a moon and a planet.

Plain Language Summary Saturn's small icy moon Enceladus interacts with the planet's magnetic field, generating intermittent aurora in Saturn's upper atmosphere and electromagnetic waves that travel along invisible magnetic connections between them. During its 13-year mission, the Cassini spacecraft repeatedly crossed these magnetic field lines linked to Enceladus. We used data from several Cassini instruments to study how energy and particles move between the moon and Saturn. We detected wave activity characteristic of Alfvén waves (similar to vibrations on a string), forming as Saturn's magnetic field flows past Enceladus. Due to a complex system of reflection at both Saturn's ionosphere and the boundary of Enceladus' torus, these waves were found not only near the moon but also trailing far behind it, extending more than 504,000 km (over 2,000 times the moon's radius) behind it. This is the first time that Alfvén waves have been observed to be directly linked to the charged particles associated with Enceladus. This shows that Enceladus plays a much bigger role in shaping Saturn's space environment than previously thought, and reveals how moons can influence their host planet across vast distances.

1. Introduction

The electrodynamic interaction between magnetized planets and their moons, whenever electrically conductive, plays a fundamental role in shaping magnetospheric dynamics throughout the Solar System. Since the mid-20th century, with the discovery of the Io-Jupiter interaction from the ground-based detection of powerful decametric emissions (Bigg, 1964), it has been recognized that such interactions are often mediated by Alfvén waves, which transfer energy and momentum along magnetic field lines connecting moons and their host planet. Early theoretical work considered Alfvén waves primarily as current carriers (Drell et al., 1965), but subsequent spacecraft observations, particularly from Voyager and Galileo, have revealed that these waves undergo reflection, cascade to smaller scales, and accelerate particles (Belcher et al., 1981; Chust et al., 2005; Hess et al., 2010). These findings motivated the development of more advanced theoretical models that account for the complex plasma interactions, including Alfvén wing formation, field-aligned currents, and the presence of negatively charged dust grains (e.g., Neubauer, 1980; Saur, 2004; Saur et al., 2007; Simon et al., 2011).

Among all planetary systems, the Io–Jupiter interaction remains the most efficient characterized example of Alfvénic coupling, thanks to extensive observations made during the Voyager, Galileo, and Juno missions, as well as those made using space telescopes and ground-based radio measurement campaigns. These missions revealed that Alfvén waves generated by Io (Kivelson et al., 1996) undergo reflections (Bonfond et al., 2008, 2009), filamentation into smaller scales (Chust et al., 2005; Hess et al., 2010; Sulaiman et al., 2023, 2024), and coupling with energetic particle populations along Jupiter's magnetic field lines (Gérard et al., 2006; Gershman et al., 2019; Szalay et al., 2018), producing complex auroral signatures at high latitudes (Bonfond, Gladstone, et al., 2017; Clarke et al., 2002; Hess et al., 2011). The moon–magnetosphere interaction also generates intense radio emissions, most notably the Io decametric emission, produced by the cyclotron maser instability (Hess et al., 2007; Louis et al., 2023; Zarka, 1998). Multiple auroral spots have been identified and linked to distinct features of the interaction, including the main Alfvén wing (MAW), reflected Alfvén Wings (RAWs), and trans-hemispheric electron beams (TEB) (Bonfond, Grodent, et al., 2017; Bonfond & Sulaiman, 2024; Clarke et al., 1996; Connerney et al., 1993; Hue et al., 2023; Prangé et al., 1996). These observations have firmly established the role of Alfvén waves not only as current carriers but also as dynamic agents of particle acceleration and energy transfer across planetary magnetospheres. Similarly to the thorough observation of the Jovian system, Cassini observations have demonstrated that Enceladus drives comparable complex and large-scale electromagnetic interactions within Saturn's magnetosphere.

In contrast to Jupiter, Saturn's magnetosphere is less dynamic, and its moons were initially thought to produce less variable electromagnetic interactions. This difference mainly arises because Saturn's magnetic dipole is closely aligned with its rotation axis, resulting in relatively stable magnetic fields in the moon's orbits. Consequently, temporal magnetic field variations near these moons are limited, resulting in weaker induced magnetic fields within them, unlike the key driver of electromagnetic interactions at Jovian moons such as Europa and Callisto (Khurana et al., 1998; Kivelson et al., 1999). However, this view was revised following the discovery of a dense water group ion cloud emanating from cryovolcanic activity at Enceladus' south pole (Dougherty et al., 2006; Porco et al., 2006). Despite its modest radius ($R_E \sim 252$ km), Enceladus acts as a significant conductive obstacle to Saturn's plasma flow, generating Alfvén wings (Jia et al., 2011; Saur et al., 2007), distorting the magnetic field, and altering local plasma conditions through mass loading and dust interactions (Kriegel et al., 2011; Simon et al., 2011). These processes lead to electron absorption and conductivity changes that produce asymmetric wave structures and complex phenomena such as anti-Hall effects, revealing a far more intricate and dynamic electromagnetic environment than previously anticipated. Recently, Alfven wings have also been observed at Titan (Kim et al., 2024).

The Cassini spacecraft, which orbited Saturn from 2004 to 2017, offered a unique opportunity to investigate the electromagnetic coupling between Saturn and its moon Enceladus. The various in situ and remote sensing instruments detected multiple signatures of this interaction, including magnetic field perturbations, field-aligned currents, radio waves and auroral emissions magnetically connected to Enceladus. Magnetic field measurements from the Cassini magnetometer (MAG) revealed perturbations associated with Enceladus' interaction with the surrounding plasma, including bending and draping of magnetic field lines around the moon, features indicative of Alfvén wing formation, characteristic of sub-Alfvénic plasma interactions (Dougherty et al., 2006; Jia et al., 2011). Concurrently, energetic particle observations from the Magnetospheric Imaging Instrument/Low Energy Magnetospheric Measurement System (MIMI/LEMMS) identified regions of ion depletion and electron

absorption near Enceladus' orbit (Jones et al., 2006; Roussos et al., 2005, 2007). These recurrent flux depletions, or microsignatures, co-rotate with Saturn and remain fixed in magnetic longitude, providing evidence that Enceladus and its dense neutral plume act as a localized and persistent sink for energetic particles within Saturn's magnetosphere. Similar flux depletions were observed in the thermal electron population by the Cassini Plasma Spectrometer Electron Spectrometer (CAPS/ELS), consistent with absorption by cold plasma or interactions with charged dust grains in the plume (Tokar et al., 2006). Complementing these observations, the Radio and Plasma Wave Science (RPWS) instrument and CAPS/ELS detected auroral hiss whistler-mode waves near Enceladus, accompanied by weakly energetic (1–50 eV) field-aligned electron beams (Gurnett et al., 2011; Leisner et al., 2013). These emissions are interpreted as signatures of parallel electric fields and standing Alfvén wave structures close to the moon. Similar hiss emissions were later observed at higher latitudes during Cassini's final orbits, mapping to magnetic field lines connected to Enceladus, demonstrating that this coupling extends vertically from the moon to Saturn's ionosphere (Sulaiman et al., 2018). Moreover, Engelhardt et al. (2015) conducted a detailed joint analysis of RPWS Langmuir Probe (LP) and MAG data to examine the structure of Enceladus' plasma and dust environment. Their study identified several distinct plasma regions, including a charged dust trail downstream of the moon and a sharp boundary at the edge of the plumes. They also reported strong field-aligned currents at the geometrical edge of Enceladus, highlighting the active electrodynamic processes operating in its near-space environment. Furthermore, the field-aligned electron beams observed by CAPS/ELS were shown to be of sufficient intensity (kinetic energy flux) to generate aurora, and this prediction motivated the targeted remote sensing search from the Ultraviolet Imaging Spectrograph (UVIS). The UVIS observations then confirmed the presence of a localized auroral spot in Saturn's upper atmosphere that is magnetically connected to the moon's position (Pryor et al., 2011), providing the first direct evidence of a large-scale electromagnetic coupling between Enceladus and Saturn. This auroral feature is interpreted as precipitating electrons accelerated along magnetic field lines intersecting the Enceladus interaction region, confirming the existence of a current system linking the moon to Saturn's ionosphere. However, over 13 years of the Cassini mission, UVIS has detected the auroral spot only four times in total in the northern hemisphere and showed to produce a very weak and highly variable ultraviolet emission brightness between 0.2 and 1.5 kR (Pryor et al., 2024). Interestingly, no radio emissions of auroral nature, such as those induced by Io (Bigg, 1964), Europa or Ganymede (Louis et al., 2017; Zarka, P. et al., 2018), have been detected so far, supporting the fact that the Saturn-Enceladus electrodynamic interaction drives weak and transient electromagnetic emissions.

While these studies collectively show that Enceladus can drive electrodynamic interactions as strong and complex as those at Jupiter, all the reported in situ observations have been limited to targeted flybys or highly inclined orbits such as the Grand Finale, leaving much of Cassini's flux tube crossings connecting Enceladus to Saturn unexplored. In this study, we combine data from Cassini's in situ fields and particle suites to perform a comprehensive investigation of the Alfvénic interaction between Enceladus and Saturn. By exploiting all available data from the orbital phase of the mission, we focus in particular on identifying and characterizing Alfvén waves and their evolution along Enceladus' flux tube and orbit. After describing the instruments and methodology, we present the statistical results of the alfvenic signatures. We then discuss specific case studies and conclude with a discussion.

2. Instrument Description and Methodology

We utilize four in situ instruments onboard the Cassini spacecraft, providing complementary measurements of electromagnetic fields and particles. Data availability varies across encounters due to operational constraints, and our analysis is therefore based on available coverage from each instrument.

The Cassini fluxgate magnetometer measures three components of the magnetic field over a wide dynamic range spanning from DC to 32 Hz (Dougherty et al., 2004). In this study, we use MAG data to resolve vector magnetic field fluctuations crucial for identifying Alfvénic wave signatures and field-aligned current systems. To isolate wave perturbations, the mean background field is subtracted, and the data are transformed into a magnetic field-aligned (MFA) coordinate system. This transformation enables decomposition into transverse (incompressible) and parallel (compressional) components and allows characterization of the wave polarization.

The RPWS instrument consists of five receivers, a Langmuir Probe, three electric antennas used here as a combination of a dipole antenna (Ex) and an orthogonal monopole antenna (Ew), and a triaxial search-coil magnetometer (see Gurnett et al., 2004)) for a detailed description of the instrument). The receivers cover a

range from ∼1 Hz to 16 MHz for electric fields, and ∼1 Hz to 12 kHz for magnetic fields. This study will primarily use the wide-band receiver (WBR), and the five-channel waveform receiver (WFR). The WBR obtains waveforms from one sensor (usually the Ex electric antenna) in one of two frequency bands, either 60 Hz to 10.5 kHz, or 800 Hz to 75 kHz. The duty cycle of the WBR ranges from nearly continuous to a few snapshots per day depending on the available telemetry. The WFR obtains simultaneous waveforms from up to five sensors in one of two frequency bands, either 1 to 26 Hz, or 3 Hz to 2.5 kHz. The WFR is usually operated with the Ex dipole, Ew monopole, and the three search coil magnetometers (Bx, By, Bz). The instrument's sensitivity and broad frequency coverage allow distinguishing between electrostatic waves, characterized by electric field fluctuations much larger than magnetic fluctuations ($\delta E \gg c\,\delta B$), and electromagnetic waves where electric fluctuations are smaller or comparable to magnetic fluctuations ($\delta E \leq c\,\delta B$).

The Electron Spectrometer (ELS), a part of the Cassini Plasma Spectrometer (CAPS), is a hemispherical electrostatic analyzer designed to measure electron fluxes as a function of energy-per-charge and arrival direction (Young et al., 2004). It covers an energy range of 0.8 eV–27 keV with a 160° field of view. Since Cassini was a three-axis stabilized spacecraft, CAPS was mounted on rotating platforms enabling the sensors to turn and collect data from various directions, providing comprehensive coverage of the pitch angle distribution of the electrons and the ions. As CAPS operations ceased in 2012, ELS data are available for a subset of flybys.

The LEMMS sensor of the MIMI instrument, measures energy spectra and pitch angle distributions of electrons (15 keV–1 MeV) and ions (30 keV– several MeV) using two oppositely oriented telescopes (Krimigis et al., 2004). The High- and Low-Energy Telescopes (HET and LET) allow measurements of particle anisotropies and depletions associated with the plasma environment near Enceladus. In this study, LEMMS is used to identify energetic particle signatures coincident with wave activity associated to Enceladus flux tube.

The first step in this study involves identifying time intervals during which Cassini observed signatures of electrodynamic coupling between Enceladus and Saturn. All available orbits were examined and periods were selected when the spacecraft was (a) within a magnetic L-shell range encompassing Enceladus' orbit ($L = [3.85-4.10]$ with Enceladus' apoapsis and periapsis being 3.97 R_S and 3.93 R_S, respectively) and (b) within a relative longitude to Enceladus ($\Delta\lambda$) between 0° and +180°, thus ensuring favorable geometries for detecting potential interaction signatures downstream of the moon. Periods beyond 180° longitude were also examined; however, only pickup ion cyclotron waves were detected, with no evidence of Alfvénic perturbations. For each selected interval, we analyzed magnetic field data from the fluxgate magnetometer onboard the Cassini spacecraft, in the Magnetic Field Aligned coordinate system to characterize wave activity by performing a quantitative spectral analysis. Alfvénic perturbations were identified based on enhanced transverse ($\delta B_\perp$) fluctuations, minimal variation in the field-aligned ($\delta B_\parallel$) component, and an approximately constant total magnetic field magnitude ($|\mathbf{B}|$), consistent with the behavior of incompressible Alfvén waves. Since the MAG instrument was the only one operating continuously throughout the mission, it forms the foundation for event selection and characterization of the Alfvénic perturbations.

3. Observations

3.1. Spatial Distribution of the Alfvénic Signatures

Based on the event selection methodology outlined in the previous section, we identified 127 events magnetically connected to Enceladus or its plasma torus. Of these, 36 intervals exhibit clear Alfvénic perturbations in the MAG instrument data, including all of the targeted flybys of Enceladus. It should be noted that nearly one-third of these cases (13 events) correspond to non-flyby cases and had still been unreported.

The spatial distribution of all the identified events is shown in Figure 1, where they are marked in magenta along the Cassini orbits and labeled by the corresponding day of year (DOY). We note that the DOY are all unique, the reason for which they are used as labels. Light blue curves indicate targeted flybys of Enceladus, while dark blue curves represent newly identified, non-flyby cases. For completeness, we also include three high-inclination orbits (shown in orange) during which auroral hiss (DOY 245 and 332) and electron beams (DOY 182 and 332) magnetically connected to Enceladus were reported by Sulaiman et al. (2018) and Rabia et al. (2025). Periods during which Cassini traversed the plasma torus' L-shell without detecting any signatures of electrodynamic interaction are shown in gray. As illustrated in Figures 1a, 1c, and 1d, the events in magenta align well

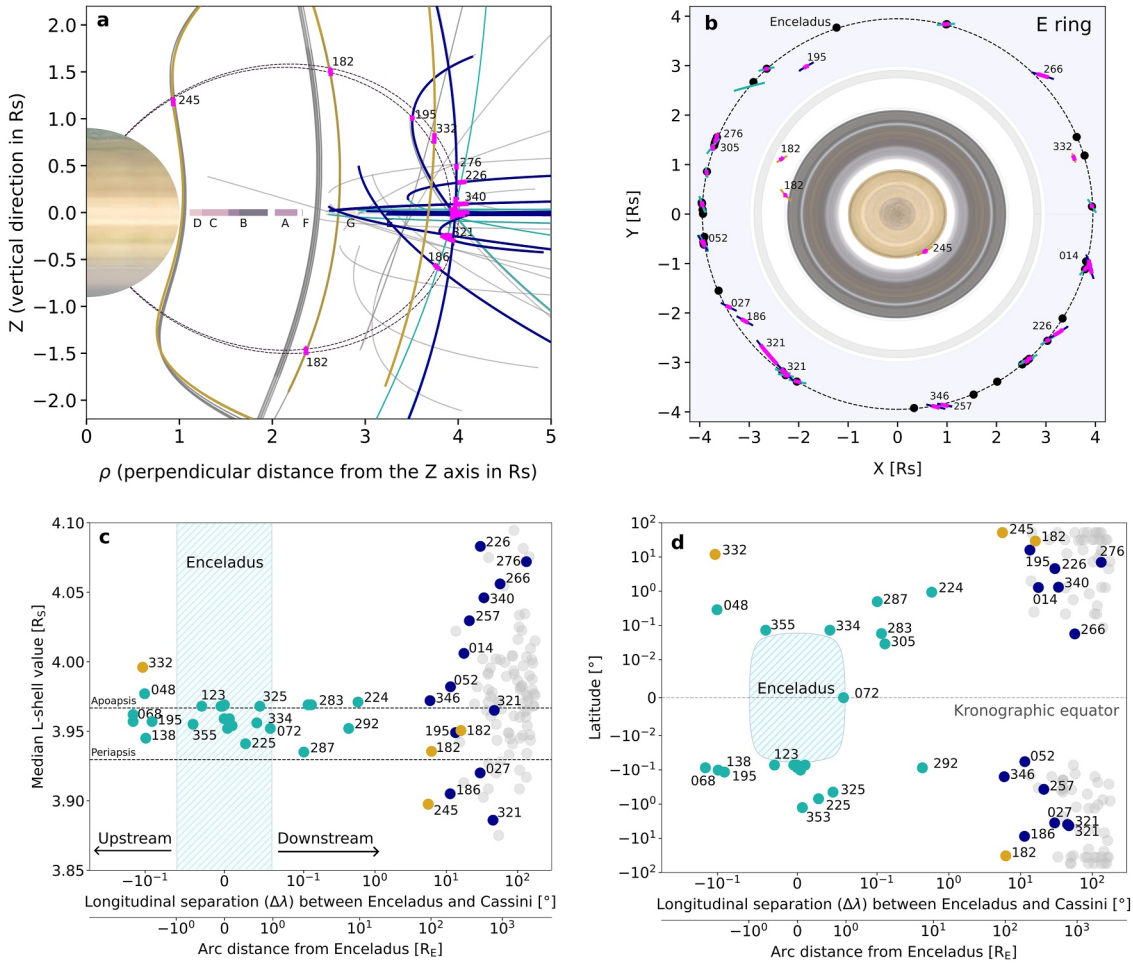

Figure 1. Spatial distribution of the identified events exhibiting Alfvénic perturbations that are connected to Enceladus (highlighted in magenta). Panels (a) and (b) show Cassini's trajectory in the meridional (ρ-Z) and equatorial (XY) planes, respectively, in units of Saturn radii (1 R_S = 60,268 km). The coordinate system is the Saturn solar equatorial system with X defined as being along the planet-Sun axis and positive toward the Sun, Z defined as the northward spin axis of Saturn, $Y = Z \times X$, and $\rho = \sqrt{X^2 + Y^2}$. Light blue curves denote targeted Enceladus flybys (E01–E21), while dark blue curves indicate newly identified events from non-flyby paths. Orange curves denote high-latitude passes with evidence of auroral hiss and electron beams recorded by RPWS and CAPS/ELS respectively (Rabia et al., 2025; Sulaiman et al., 2018). The gray curves indicate intervals that satisfied the selection criteria but exhibited no discernible signatures of electrodynamic coupling with Saturn. The magenta color denotes the periods of Alfvénic perturbations. The black dashed curve in panel (a) indicates the magnetic flux tube connecting Enceladus to Saturn; in panel (b), it shows Enceladus' orbital path. Each of the black dots in panel (b) represents the position of Enceladus for each event. Panel (c) and (d) present the median L-shell values and latitudes respectively, as a function of the spacecraft-moon longitude separation angle ($\Delta\lambda$) at the start of each interval and the corresponding distance from Enceladus. Horizontal dashed lines in panel (c) mark Enceladus' apoapsis (3.97 R_S) and periapsis (3.93 R_S). The light blue shaded and hatched area in panels (c) and (d) represents the section of Enceladus. Numbers correspond to the Day of Year (DOY) for each event; for clarity, only a subset of targeted flybys is labeled.

with the downstream magnetic L-shell of Enceladus, and Figure 1b shows their alignment along the orbital path of the moon except for the highest latitude events.

Figure 1 demonstrates that the selected events span a wide range of latitudes and longitudes in both hemispheres, indicating that the Alfvénic activity associated with Enceladus is not limited to a localized region but extends far downstream, up to $\sim 133^\circ$ (~ 2185 R_E). This suggests a broad electrodynamic interaction region and the existence of an Alfvén wing system extending far downstream of the moon. This could occur very likely via reflection of the Alfvénic waves, not only at Saturn's ionosphere, but also on the Enceladus plasma torus boundary. The L-shell distribution (Figure 1c) further shows that while most events fall within the radial range of Enceladus' orbit, bounded by its periapsis and apoapsis (horizontal dashed lines), several non-flyby events occur outside this range. These outliers are associated with higher $\Delta\lambda$, particularly at separations exceeding 10° (or ~ 165 R_E), suggesting that the plasma torus of Enceladus becomes more radially extended and diffuse at greater distances from its plumes. Furthermore, beyond a longitudinal separation of 10°, numerous events (shown in gray in

Figures 1c and 1d) traversed Enceladus' L-shell including its plasma torus without exhibiting any signatures of electrodynamic interaction with Saturn. This absence of signature, may indicate sharp spatial variabilities within the Alfvén wing current system of Enceladus. Further interpretation of these variabilities and characteristics is provided in Section 4.

3.2. Case Study Analysis

In this section, we present case studies illustrating the electrodynamic interaction between Enceladus and Saturn, with a primary focus on the characterization of Alfvénic perturbations using magnetic field measurements from the MAG instrument. When available, these observations are complemented by electric field data from the RPWS experiment and by electron measurements from the CAPS/ELS and MIMI/LEMMS sensors, providing a multi-instrument perspective on the coupling processes.

3.2.1. Non-Flyby Events: Examples of Reflected Alfvén Wings

We first present a set of six representative cases, which are not associated with moon flybys, selected to span a broad range of latitudes and longitudes. These events are shown in Figure 2, with additional cases provided in the Supplementary Material (Figures S1–S7 in Supporting Information S1). For each case, we display (from top to bottom): (a) the magnetic field magnitude and components in the Kronocentric Radial–Theta–Phi (KRTP) coordinate system, (b) the transverse (non-compressive) and parallel (compressive) magnetic field perturbations relative to the background mean magnetic field (for visualization purposes we plot $\delta B_{\parallel}/3$), (c) and (d) their corresponding power spectral density (PSD), respectively, with overlaid proton $\left(f_{cH^+}\right)$ and water-group ion cyclotron frequencies (f_{cW^+}, for a range of mass-to-charge, m/q, ratios). The KRTP coordinate system is a Saturn-centered spherical coordinate system where R is the radial direction pointing outward from Saturn, θ is the meridional direction (pointing southward from the north pole), and ϕ is the azimuthal direction (in the direction of Saturn's rotation). Panel A (DOY 195) and Panel B, (DOY 276) are two examples of events that include simultaneous low-energy electron differential energy flux from CAPS/ELS along with Alfvénic magnetic field signatures (other examples are shown in the Supplementary Material). The event during DOY 195 is part of Cassini's second flyby of Enceladus in 2005. Following a close encounter through the southern hemisphere plume, the spacecraft re-crossed magnetic field lines connected to Enceladus at higher northern latitudes during its outbound trajectory (see Figure 1a). A detailed analysis of ELS data from this event is presented in Rabia et al. (2025). The event during DOY 276, is the farthest case downstream of the moon ($\Delta\lambda = 133°$) exhibiting sharp gradients in the perpendicular components of the magnetic field along with electron beam signature.

All these identified events exhibit weak (compared to Io/Jupiter case) magnetic field perturbations lasting approximately 4 minutes (shaded in gray), with power concentrated at frequencies below the local f_{cH^+}. These fluctuations are predominantly transverse to the background magnetic field (orange and green traces), with minimal variation in the field-aligned (parallel) direction, as confirmed by the corresponding PSDs (c and d). The observed incompressibility is consistent with magnetohydrodynamic Alfvén waves (and their extension to higher frequencies) propagating along the field lines. In addition to these Alfvénic signatures, several events (B, D, E, and F) show distinct narrow-band wave activity near ion cyclotron frequencies extending before and after the period of the Alfvénic perturbations. The enhanced wave power aligns with m/q corresponding to water-group ions created by photo-ionization of the neutral exosphere surrounding the E-ring material (Tokar et al., 2006, 2009): O^+ ($m/q = 16$), OH^+ ($m/q = 17$), H_2O^+ ($m/q = 18$), H_3O^+ ($19 \leq m/q \leq 23$), and heavier water cluster ions such as $(H_xO_2)^+$ ($36 \leq m/q \leq 42$). These pick-up ion cyclotron waves are consistent with previous reports of such waves within the E ring (Leisner et al., 2006). Further supporting the interpretation of extended interaction, cases A, C, D, and E exhibit pronounced dropouts in energetic electron fluxes (typically 20–100 keV) as observed by MIMI/LEMMS. Similar dropouts have been previously reported near Enceladus and at other icy moons such as Tethys, Dione, and Rhea (Andriopoulou et al., 2014; Jones et al., 2006; Roussos et al., 2005, 2007). They are attributed to the absorption of the energetic electrons by the neutral and dusty environment of the moon. The occurrence of these dropouts far downstream of Enceladus, across a wide range of latitudes, suggests the presence of a spatially extended electron wake. In some events (notably D and E), the energetic electron depletions are shifted from the observed Alfvénic wave activity by several minutes. This timing offset may result from differences in drift paths between energetic electrons and the bulk plasma population. In cases where no clear

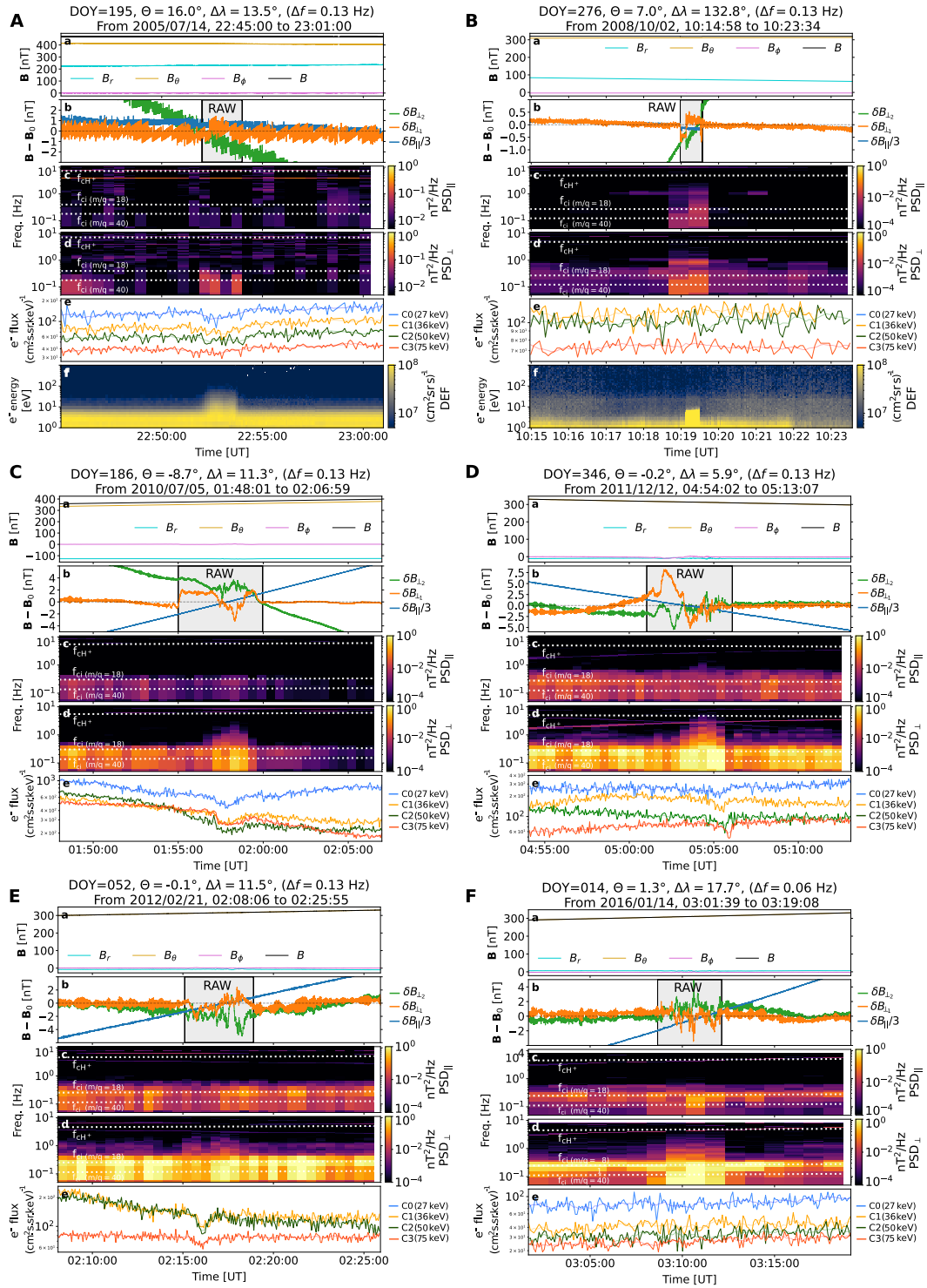

Figure 2. Examples of non-flyby paths exhibiting reflected Alfvénic perturbations plausibly correlated to the moon's position. For each of them, from top to bottom, panels show: (a) magnetic field components in KRTP coordinates from MAG; (b) perturbed magnetic field components in the Magnetic Field Aligned coordinate system (where $\mathbf{B}_0$ represents the background magnetic field). For visualization purposes we plot $\delta B_{\parallel}/3$; (c) PSD of parallel magnetic field fluctuations; (d) PSD of perpendicular magnetic field fluctuations; (e) energetic electron fluxes from MIMI/LEMMS; and (f) low energy electron differential energy flux from CAPS/ELS, when available. Horizontal dashed lines indicate the proton gyrofrequency $\left(f_{cH^+}\right)$ and the gyrofrequencies of water-group ions with mass-per-charge ratios of $m/q = 18$, and 40. The gray shaded area in panel b represents the interval during which a RAW is observed.

dropout is observed, this could come from temporal variability or from limitations in pitch-angle coverage, which can influence the detectability of these features (Roussos et al., 2007).

These case studies provide the first in situ evidence that Enceladus' electromagnetic interaction with Saturn, although weak, extends significantly downstream of the moon. This is supported by the detection of Alfvénic perturbations and indirect signatures of water-group ions well beyond Enceladus' flux tube. We interpret the Alfvénic perturbations as reflected Alfvén wings (RAWs), analogous to those observed in the Io–Jupiter electromagnetic interaction. The presence of an energetic electron depletion at large longitudes and high latitudes further indicate the persistent nature of the broad and complex Enceladus-Saturn system (see Section 4).

3.2.2. Enceladus Northern Targeted Flyby: A Main Alfvén Wing Example

In addition to examples from non-flyby paths, Figure 3 presents a case study from a close encounter with Enceladus in the northern hemisphere (E12 flyby on 30 November 2010, DOY 334). This event is particularly valuable, as it provides comprehensive wave coverage across a broad frequency range, including the full dynamic range of the instrument. Alongside low-frequency magnetic field data from the MAG instrument, higher-frequency electric and magnetic field measurements from the RPWS/WFR (up to 10 Hz) and RPWS/WBR (up to 80 kHz) are also available (Figure 3a). A second example with similarly comprehensive wave coverage is shown in Figure S8 in Supporting Information S1 (E20 flyby: 14 October 2015, DOY 287). The Cassini trajectory during this flyby is shown in Figure 3b, in the Enceladus Interaction System (ENIS), where the *X*-axis is aligned with the direction of corotation, the *Y*-axis points toward Saturn, and the *Z*-axis completes the right-handed coordinate system in the local south–north direction. As Cassini passed near Enceladus (with a closest approach at 11:53:59 around 1.15 R_E from the moon's center), clear rotations in the transverse magnetic field components were observed (Figure 3a, panel b), suggesting the presence of a field-aligned current at or near the magnetic flux tube connected to the moon (Engelhardt et al., 2015). The corresponding PSDs in panels c and d reveal the spectral structure of this flux tube. While low-frequency field-aligned currents are concentrated at its edges, higher-frequency waves, particularly up to almost f_{cH^+}, are largely present, between 11:48 and 12:00 UT, on its extended border. Unlike the interior, where such wave activity is clearly absent. Given that Cassini was magnetically connected to Enceladus during this interval, these signatures correspond to the MAW (Jia et al., 2011). As in the previous non-flyby cases, narrowband emissions consistent with water-group ion cyclotron waves are also present before and after the flux tube crossing.

Despite the typically noisy environment around the Search-Coil Magnetometer (SCM), rare and useful high-frequency magnetic field data were available for this case, and confirm the trend observed by the MAG instrument for the part covering the same frequency range. Panels e and f of Figure 3a show that transverse magnetic perturbations dominate above f_{cH^+}. Interestingly, the parallel electric field power (panel g) decreases above f_{cH^+}, while the perpendicular electric field power increases (panel h), suggesting that the Alfvénic fluctuations extend into magnetosonic or whistler-mode waves above the proton gyrofrequency. Although the explanation for this phenomenon is unclear (the fact that a large-scale Alfvénic disturbance is systematically associated with small-scale fluctuations), we suggest the possibility of a turbulent filamentation/fragmentation process of the Alfvén wing disturbance during its propagation or its decay by current-driven wave instabilities. We note here that since the electric field is only 2D the perpendicular and parallel directions are defined with respect to the projection of the background magnetic field onto the Ex-Ew antenna plane. Also, the horizontal narrow-band emissions around 6 and 8 Hz (panels e and f) are noise signals detected by the SCM from the reaction wheels or electrical systems on the spacecraft. At even higher frequencies, electric field measurements from the WBR reveal highly structured emissions (panel i), with a zoom shown in Figure 3c. Notably, a series of auroral hiss emissions are observed below the electron cyclotron frequency (f_{ce}), manifesting as sharp-edged, funnel-shaped structures in the dynamic spectrum (Gurnett et al., 2011; Sulaiman et al., 2018). The first, centered at 11:53:27 UT, extends up to approximately 3 kHz and fades near 5 kHz. A second, much weaker emission appears at about the same time, restricted to higher frequencies. The final and most complex set occurs at 11:54:35 UT, composed of multiple stacked funnels. These features were previously reported and analyzed in details by Leisner et al. (2013), who attributed them to field-aligned currents near Enceladus' surface. The spatial mapping of these emissions (yellow stars in Figure 3b) confirms their origin close to the moon. The broadband spikes that appear concurrently with the funnel, likely represent noise from dust impacts as Cassini traversed the dense environment near the moon.

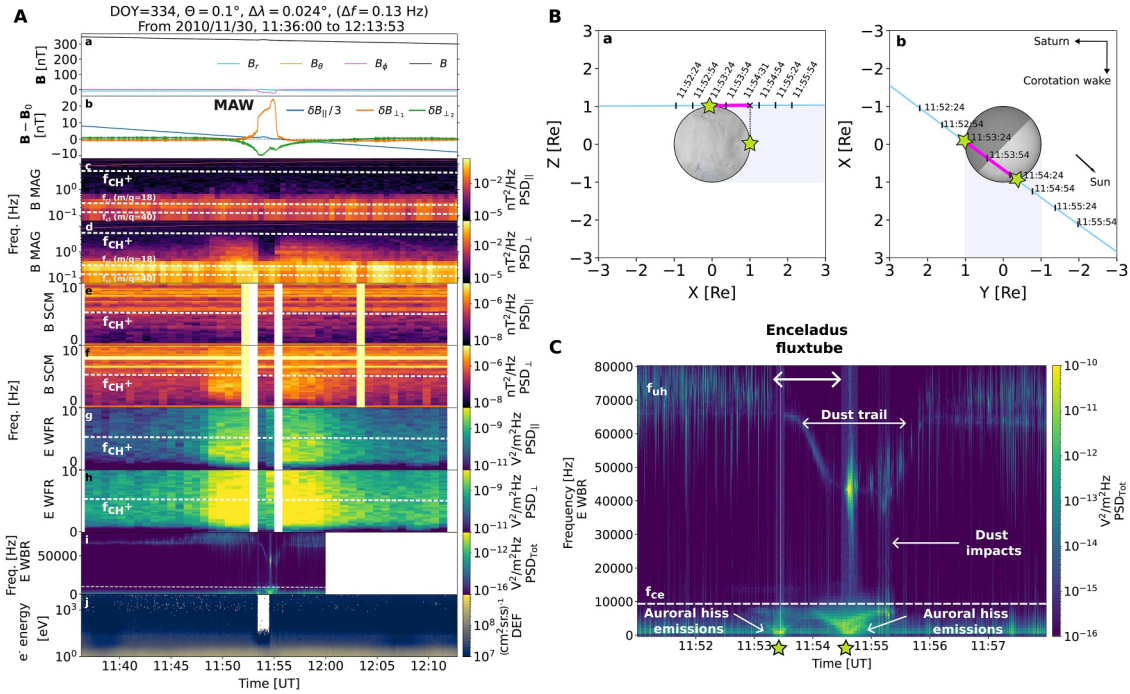

Figure 3. Example of a targeted Enceladus flyby (E12). (a) Fields and plasma parameters: panels (a–d) are as in 2; panels (e) and (f) show the power spectral densities (PSDs) of the parallel and perpendicular magnetic field fluctuations from RPWS/SCM at higher frequencies than MAG. Panels (g) and (h) present the PSDs of the parallel and perpendicular electric field components from RPWS/WFR, while panel (i) shows the PSD of the total electric field from RPWS/WBR. Panel (j) displays the energy–time spectrogram of the electron differential energy flux from CAPS/ELS. (b) Cassini's trajectory in the Enceladus–Interaction System (ENIS) coordinate system. (c) Zoomed-in view of the electric field data from RPWS/WBR.

In addition, a well-defined spectral band is also observed near the upper hybrid resonance frequency, $f_{uh} \sim 75$ kHz. The upper hybrid frequency is given by $f_{uh} = \sqrt{f_{ce}^2 + f_{pe}^2}$, where f_{ce} is the electron cyclotron frequency and $f_{pe} = 9\sqrt{n_e}$ kHz is the electron plasma frequency, with n_e representing the local electron number density in cm^{-3}. The value of f_{uh} thus depends on both the local magnetic field strength and the local electron density (Dougherty et al., 2006; Persoon et al., 2020). This band exhibits a distinct spectral profile, characterized by a narrow-band core and a more variable broadband extension toward higher frequencies. The latter may result from thermal plasma effects (Tokar et al., 2006). Of particular interest is the dip in f_{uh} observed between 11:53:24 UT and 11:56:00 UT, coinciding with the flux tube crossing and extending further in the downstream region. This feature indicates a region of electron depletion (and constant ion densities), previously reported by (Engelhardt et al., 2015) as dust trail region, likely caused by enhanced dust densities in the E-ring wake of Enceladus, which efficiently collect electrons but not ions. Finally, persistent broad-band emission peaking near 45 kHz around 11:54:30 UT is detected during the outbound leg of the flyby. This may correspond to upper hybrid oscillations driven by electron beams associated with auroral hiss activity at lower frequencies.

4. Discussion

4.1. Geometry of the Main and Reflected Alfvén Wings

These observations illustrate key features of sub-Alfvénic moon–magnetosphere interactions, where the relative flow velocity between a moon and the surrounding plasma is nominally lower than the local Alfvén speed generating electromagnetic waves propagating along the magnetic field lines from the moon to Saturn's ionosphere, instead of a bow-shock, and forming the so-called main Alfvén wing (MAW) current system. At Enceladus' orbital distance of ∼4 R_S, the moon travels at about 12.6 km/s, while the magnetospheric thermal plasma moves at about 39.0 km/s, overtaking the moon at a speed of $v_0 \approx 26.4$ km/s (e.g., Saur, 2021; Tokar et al., 2006). With typical field strengths (330 nT) and plasma mass densities ($n_i \sim 50$ cm^{-3} and $m_i \sim 18$ amu), the Alfvén speed is estimated at $v_A \sim 200$–300 km/s, resulting in an initially shallow but finite Alfvén wing angle

of $\alpha = \tan^{-1}(v_0/v_A) \sim 5.0°$–$7.5°$, near the moon. By using most accurate available magnetic field and plasma density models (Dougherty et al., 2018; Persoon et al., 2020), we next examine the geometry of the dynamical extension of the MAW. We calculated the travel time of an Alfvén wave perturbation launched from Enceladus to Saturn's northern ionosphere along Saturn's magnetic field line, as a function of latitude (Figure 4). The red and blue curves in Figure 4a represent the radial distance in spherical coordinates reached by the Alfvénic perturbation, and the corresponding curvilinear distance along the field line, respectively. The Alfvén speed profile (Figure 4b) was calculated using the symmetric (north-south) distribution of the ion density of the water-group from the diffusive equilibrium model of Persoon et al. (2020) combined with the magnetic field octupole model derived from Dougherty et al. (2018). At Enceladus (latitude $\Theta = 0°$), the Alfvén speed is $v_A \approx 260$ km s^{-1} and increases by a factor 2 near $\Theta \approx 6°$ (by an order of magnitude near $\Theta \approx 12°$). A second sharp increase at $\Theta \approx 35°$ is due to the absence of ion density constraints at high latitudes, marking the upper limit of the density model; beyond this point, v_A is assumed to equal c, the speed of light. The travel time profile (Figure 4c) shows that between the equator and $\Theta \approx 6°$, the Alfvén wave travel time increases roughly linearly with latitude, requiring $\sim$80 s to reach $\Theta = 6°$. As Saturn rotates relative to the orbital motion of Enceladus at frequency $\approx$0.00634°/s, this corresponds also to a longitudinal displacement of $\sim$0.51° (i.e., $\sim$8 R_E in the orbital plane). Beyond $\Theta \approx 10°$, most of the field-line path is traversed very quickly ($\sim$15 s), and the Alfvén wave reaches Saturn's northern ionosphere at $\Theta \approx 63.4°$ N with a downstream longitudinal displacement of $\sim$0.73° ($\approx$12 R_E). This geometry implies that after one reflection at the ionosphere, the MAW would re-intersect the equatorial plane $\sim$24 R_E downstream from the moon. This estimated distance should be considered as a first approximation, as it is subject to uncertainties in the diffusion equilibrium model used to evaluate the Alfvén wave travel time. Numerical modeling is needed to refine this calculation. Although this does not significantly affect the propagation times we have calculated in the specific case of the northern hemisphere, it should be noted that due to the slight north-south asymmetry of Saturn's magnetic field (Dougherty et al., 2018), our calculation predicts a southern footprint located at $\Theta \approx -60.7°$ S. In total, the one-way travel time τ_A for Enceladus' Alfvén wing is slightly below 2 min. For comparison, in the Io–Jupiter system, the Alfvén wave travel time ranges between approximately 2 and 12 min depending on whether Io is below or above the moon's torus (Hinton et al., 2019). The shorter travel time at Enceladus reflects the absence of a dense plasma torus. Moreover, the nearly axisymmetric configuration of Saturn's magnetic field should result in more uniform plasma conditions along Enceladus' orbit, in contrast to those at Io.

4.2. Large-Scale Alfvénic Perturbations: Poynting Flux and Total Power

To characterize how the properties of the Alfvénic interaction evolve with distance from Enceladus (both in latitude and longitude), we first examined the evolution of the large-scale perturbations at frequencies <0.1 Hz by computing the Alfvén wave Poynting flux S (in W/m^2) and the corresponding total power (in W). These low-frequency (large-scale) perturbations are associated with the primary source of the Alfvén wing generation. The results are shown in Figure 5. We note that no Alfvénic signatures were detected for events DOY 182 and DOY 048 (E00), likely due to poor data quality from the MAG instrument. Event DOY 332 also shows no signatures, which is expected because it occurred slightly upstream and at higher latitudes relative to the moon (see Figure 1d). Therefore, these events are excluded from this part of the analysis. We calculated S for each event using $S = v_A \delta B^2_{\perp rms}/\mu_0$ where $\delta B_{\perp rms}$ is the root mean square of the DC (<0.1 Hz) perpendicular magnetic field perturbations and μ_0 the permeability of the vacuum. The total power (P) was obtained by multiplying S by $\pi \times (1.3\,R_E)^2 \frac{B_{Ence}}{B_{obs}}$. The factor of 1.3 represents the effective radius of Enceladus, based on the observed brightness of the moon's footprint size (Saur et al., 2013) and the factor $\frac{B_{Ence}}{B_{obs}}$ accounts for the change in the flux tube cross-section between the position of Enceladus ($B_{Ence} = 330$ nT) and the observation point, consistent with magnetic flux conservation.

The calculated Poynting flux (Figure 5a) peaks in the vicinity of Enceladus, reaching $\sim 4 \times 10^{-5}$ Wm^{-2}, and decreases mainly downstream to $\sim 9 \times 10^{-9}$ Wm^{-2} within the plasma torus. The corresponding total powers (Figure 5b) range from $\sim 1.5 \times 10^7$ W to $\sim 3 \times 10^3$ W. The highest power values likely correspond to Cassini's crossings of the MAW and primary RAW. However, it should be noted that several of these events (DOYs 072, 283, 305, and 287) are located tailward, up to only about 2 R_E from the moon's center, which may suggest the presence of a dense and extended plasma wake contributing to the MAW generation. Furthermore, the most intense event, DOY 072, occurs very close to Enceladus (closest approach $\approx 1.17\,R_E$), which may account for its

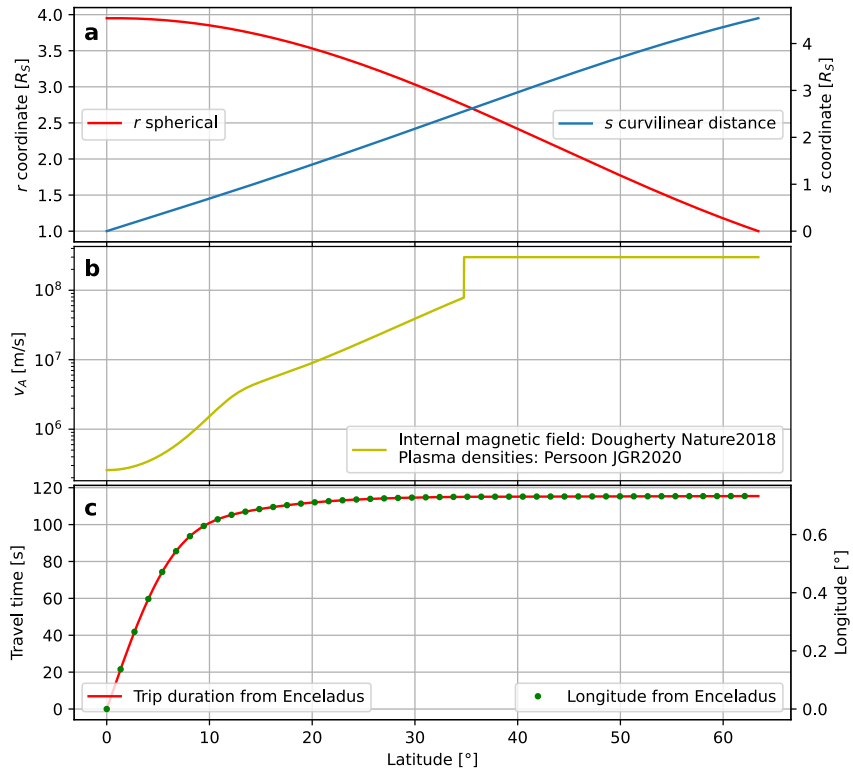

Figure 4. Evaluation of the MAW propagation geometry as a function of latitude (Θ), from equatorial plane to Saturn's northern ionosphere, for $L = 3.95$. (a) Radial distance in spherical coordinates (red) and corresponding curvilinear distance along the magnetic field line (blue). (b) Estimated local Alfvén speed, v_A, along the propagation path. (c) Alfvén wave travel time and associated downstream longitudinal displacement.

maximum power if Cassini sampled the immediate source region of the MAW within a dense plasma wake. In any case, the observed values should be taken as lower limits of the generated power and are therefore consistent with the theoretical upper limit of $\sim 2 \times 10^8$ W given by Saur et al. (2013). It is worth noting, in the interest of comparative planetology, that the total generated power at Io was also modeled (Hess et al., 2010; Saur et al., 2013) and estimated by the Juno spacecraft at Jupiter (Sulaiman et al., 2023) to be $\sim 10^4$ times stronger $(\sim 1 \times 10^{12}$ W).

At longitudinal separations greater than about 6° (~100 R_E), the power drops by more than two orders of magnitude overall. This decrease is likely caused by the multiple downstream reflections of the MAW (at the ionosphere and within the plasma torus), which disperse and dissipate the wave energy (Hess et al., 2011; Saur et al., 2013). To quantify the downstream decay of the total power, we apply an exponential fit, shown by the red line in Figure 5b. Throughout the region covered, from 0° to approximately 60° downstream, the fit works remarkably well and indicates an e-folding distance of about 7.4° (~120 R_E). Note that for the fitting, we chose to only consider events with similar characteristics and excluded two special cases from the analysis: the event that happened on DOY 245, near the planet at a very high latitude, and the event that happened on DOY 276, located furthest downstream. For comparison, in the case of Jupiter, an exponential decay has been used both theoretically and observationally to describe the UV tail emissions and the electron fluxes as a function of the down-tail angular longitudinal separation, $\Delta\lambda$, from Io, Europa and Ganymede (Bonfond, Saur, et al., 2017; Rabia et al., 2024; Szalay et al., 2020). By applying the model developed by Bonfond, Saur et al. (2017) to the present study, the exponential decay we observe can easily be explained by the partial trapping in Enceladus' torus or between Saturn's two hemispheres of the Alfvén waves generated by the moon (MAW and subsequent RAWs). During their path from one hemisphere to the other, each time the Alfvén waves reflect off the density and magnetic field gradients of the torus or Saturn's ionosphere, the Poynting flux of these waves decreases by a finite reflection coefficient $(C_R < 1)$ and thus follows a geometrical decay as they move longitudinally downstream of Enceladus. Let N be the nearest integer greater than $1/\ln(1/C_R)$. After N reflections, the wave energy flux is reduced by a

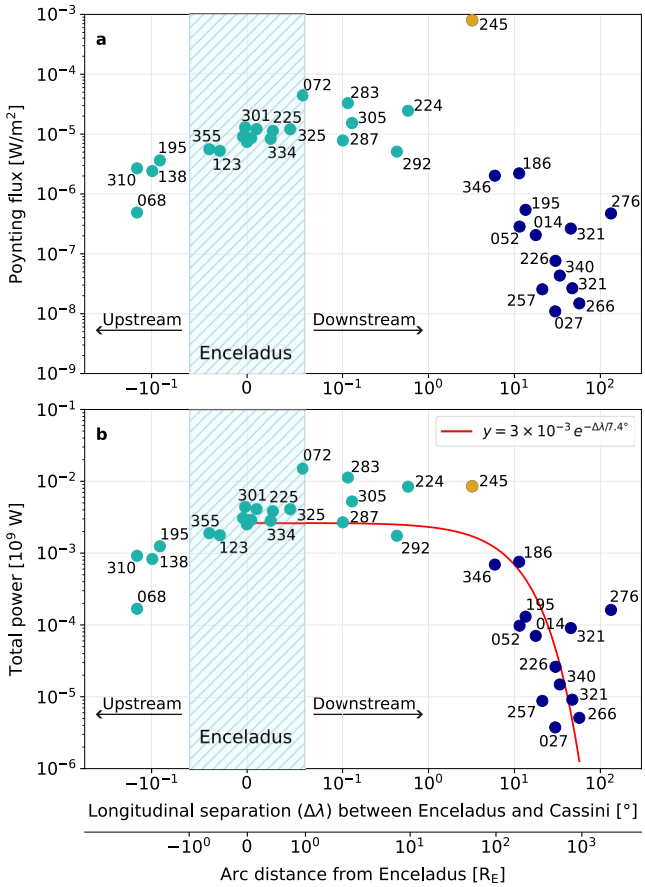

Figure 5. (a) Poynting fluxes (S) and (b) total powers measured locally for large-scale perturbations (<0.1 Hz), as a function of the moon-spacecraft longitudinal separation $\Delta\lambda$ and arc distance from Enceladus. The red line in panel (b) represents a least square fit of an exponential function.

factor slightly greater than e. As each reflection, from and back the equatorial plane, lasts $2\tau_A$, the longitudinal e-folding distance predicted for the RAWs is roughly given by:

$$\varphi_0^{\text{Alfvén}} \approx N\frac{2\tau_A v_0}{D} \quad (1)$$

with v_0 the unperturbed plasma velocity of the torus measured in Enceladus' rest frame, D the Enceladus' orbital distance, and τ_A the one-way Alfvén wave travel time from equator up to the average torus boundary or Saturn's ionosphere. For $\tau_A = 115$ s (reflection at Saturn's ionosphere), Equation 1 gives $\varphi_0^{\text{Alfvén}} = 7.2°$ with $C_R = 0.82$ corresponding to $N = 5$. For $\tau_A = 80$ s (reflection on torus boundary), we obtain $\varphi_0^{\text{Alfvén}} = 7.0°$ with $C_R = 0.87$ corresponding to $N = 7$. Both cases give similar plausible values for the reflection coefficient, consistent with the e-folding distance measured from the exponential fit.

The events occurring on DOYs 072, 283, and 224 display much higher total powers than the exponential decreasing trend. For the event on DOY 072 located near the moon, tailward, this can be explained by the presence of a particularly dense plasma wake, as previously mentioned. For the other two events, the observed high powers may be caused by a temporal variability in the MAW generation mechanism (see Section 4.6 for more details).

4.3. Small-Scale Alfvénic Perturbations: Wave Filamentation

The sharp plasma gradient associated with a moon's plasma torus has long been thought to prevent the MAW from reaching higher latitudes, where the electrons that cause the observed moon-related auroral spots are thought to be accelerated. Although a dense plasma favors the generation of an intense Alfvén wing due to the high value of the Alfvén conductance (Neubauer, 1980), a pronounced gradient in Alfvén velocity at the torus boundary will reflect most of the generated wave energy back into the torus (Wright & Schwartz, 1989). This apparent paradox was resolved by considering that the MAW had to be strongly filamented or fragmented before its first reflection by the torus boundary, as suggested from Galileo's in situ observations at Io (Chust et al., 2005) and by theoretical modeling of the wave reflection (Hess et al., 2011).

To evaluate the level of filamentation and fragmentation of the Alfvénic perturbations, we analyzed on Figure 6 the averaged PSD of the total magnetic field fluctuations in the 0.1–2 Hz frequency range during the Alfvénic perturbation period, and compared with the total power of the Alfvénic fluctuations measured at lower frequencies (DC-0.1 Hz). For greater clarity, we added on the figure the contours of the MAWs (black) and their reflections (gray) using the model shown in Figure 4. We started the downstream edge of the MAW at $2 \times R_E$ from the moon's center to take into account the plausible extended dense plasma wake of Enceladus, as suggested in the discussion of the previous section. For the sake of simplicity, the model does not take into account the extension of the conductive region by the plumes in the southern hemisphere. As shown in Figure 6a, the wave PSD peaks within 0.6° (~10 R_E) of the moon and decreases with increasing separation, persisting out to at least 120° (~2,000 R_E) downstream. In some cases, the PSD values drop by over three orders of magnitude between near- and far-regions. This spatial trend supports the interpretation that the small-scale magnetic activity originates from the MAW and its subsequent downstream reflections at the planet's ionosphere and within the plasma torus. As the MAW propagates along the field lines, likely getting partially turbulently filamented before escaping the plasma torus (Chust et al., 2005; Hess et al., 2011) and reflecting between hemispheres, it gradually disperses and dissipates, resulting in the diminished power observed at larger distances (Figure 6b).

Unlike the Galileo observations at Io, which were limited to the equatorial vicinity of the MAW, the observations presented here show a systematic correlation between the existence of large-scale Alfvénic perturbations

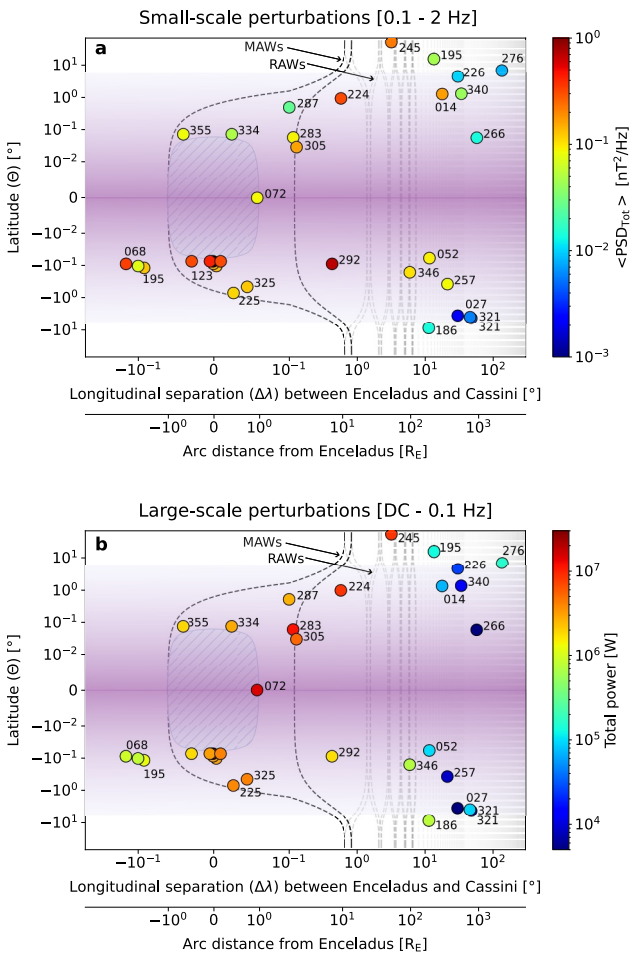

Figure 6. (a) Averaged power spectral density (PSD) of the total magnetic field fluctuations between 0.1 and 2 Hz and (b) total power of the Alfvénic perturbations at lower frequencies (DC-0.1 Hz), as a function of latitude (Θ) and the longitudinal separation between Cassini and Enceladus (Δλ) or the corresponding arc distance from Enceladus in R_E. The contours of the Main Alfvén wings (MAWs) and their reflections (RAWs) are indicated in black and gray dashed lines, respectively, for reference. The rectangular hatched area represents the section of Enceladus, and the purple cylindrical surface indicates the typical scale height of Enceladus' plasma torus as inferred by our model.

(DC-0.1 Hz) and that of small-scale magnetic fluctuations (0.1–2 Hz) at any observed distances from the moon. Thus, it could be inferred that the filamentation process occurs along the whole propagation of the MAW and its corresponding reflected parts (at Saturn's ionosphere and within the plasma torus) and not only before its first reflection as previously supposed by Chust et al. (2005) for the Io case. To complete the picture, it may be necessary to clarify the distinction between filamentation and dissipation, which are in fact two separate concepts. Filamentation in itself does not imply dissipation, but simply a conversion of scale allowing, in principle: (a) better transmission outside the torus and (b) greater dissipation via small-scale wave-particle interactions.

4.4. Inferred Scale Height of the Enceladus Plasma Torus

Based on the approximately twofold increase in v_A around 6° latitude (Figure 4), we infer a typical scale height of the Enceladus plasma torus along the field line, extending up to this latitude. This scale height, indicated in purple in Figure 6, corresponds to roughly 0.4 R_S in curvilinear distance. Furthermore, according to the predicted MAW geometry, Alfvénic perturbations are not expected at the equator within ∼24 R_E downstream of Enceladus. Nonetheless, some perturbations are observed at distances smaller than 24 R_E, such as DOY 224 and DOY 292, which can thus plausibly be explained by partial reflections of the MAW within the plasma torus over a wide range of latitudes of the density gradient (Bonfond et al., 2008; Neubauer, 1980). The presence of trans-hemispheric electron beams (TEBs), colocated with the MAW, may also generate currents along the field lines, generating additional Alfvénic perturbations. Since the statistics are limited and Cassini does not cross the region downstream between 10 R_E (0.6°) and 100 R_E (6°), the reflection of the large-scale Alfvénic waves within the plasma torus in this region cannot be confirmed.

4.5. North-South Asymmetry of the Alfvénic Signatures

The small-scale perturbations in Figure 6a exhibit a north-south asymmetry, with enhanced wave activity in the southern hemisphere within ∼10 R_E (0.6° longitude). Although this could partially reflect observational bias from Cassini's orbit, it is more likely associated with Enceladus' dense and extended southward plumes. The ionization of plume neutrals adds mass to the plasma flow, increasing velocity shear and the associated field-aligned currents of the southern MAW. This mass loading effectively increases the local plasma conductivity, thereby enhancing MAW intensity. In addition, the broad spatial extent of the southern plumes provides a larger volume over which a MAW can be generated. However, we note that the associated UV footprint has been detected only in the northern hemisphere, consistent with the generally brighter northern aurora.

Beyond 6° (∼100 R_E), the wave-power distributions become more symmetric, indicating that any plume-driven asymmetries are confined to the near-moon region. At larger scales, the perturbations shown in Figure 6b display little systematic north–south asymmetry (with a few exceptions), exhibiting only a gradual exponential decrease in total power as outlined in Section 4.2. Taken together, these observations suggest that the MAW generation is approximately symmetric to first order, while the southern water plumes primarily enhance small-scale perturbations and filamentation in the southern MAW (see Figure S9 in Supporting Information S1 for a quantitative estimate of this observation).

4.6. Temporal and Spatial Variabilities of the Alfvénic Signatures

Near the moon in the northern hemisphere, some events - such as DOY 283 (presumed to lie within the downstream extension of the MAW, see Section 4.2) and DOY 224 (plausibly located within the first reflection of the MAW on the plasma-torus boundary, see Section 4.4)- exhibit greater large-scale total powers than events occurring closer to the moon, and appear in contrast to the overall exponential trend highlighted by the red line in Figure 5b. This behavior may reflect temporal variability in the MAW generation, potentially linked to the complex and dynamic coupling between the plumes, Enceladus' ionosphere, and the surrounding plasma torus (Pryor et al., 2011). Such temporal variability could also account for the farther downstream events (DOY 245 and DOY 276) that display comparatively elevated large-scale total powers.

As pointed out at the end of Section 3.1, we expect some pronounced spatial variability when crossing the far downstream Alfvén wing current system. As a matter of fact, on DOY 321, Cassini crossed nearly tangentially the plasma torus, and two consecutive events separated by ∼15 min were observed (See Figures S2 and S3 in Supporting Information S1), which is consistent with a patchy feature of the RAW regions.

4.7. Implications for Future Enceladus–Saturn Missions

These observations are broadly consistent with the well-studied Io–Jupiter system, where strong Alfvénic coupling drives multiple auroral footprints (e.g., Bonfond, Grodent, et al., 2017). At Enceladus, our results confirm the presence of both the MAW observed at small longitudinal separations ($|\Delta\lambda| \leq 0.12°$), and RAWs extending downstream to at least ∼120° (∼2,000 R_E). However, unlike Io, only a single Enceladus auroral footprint has been detected at Saturn (Pryor et al., 2011, 2024), and no additional features linked to RAWs, TEBs or tail auroras have been observed. Due to Saturn's axisymmetric magnetic field, the phenomenology of Enceladus' auroral footprints must certainly be simpler. Nevertheless, this disparity likely reflects also the comparatively lower power of the MAW and associated electron beams at Enceladus, which may fall below the detection thresholds of Cassini's UV and plasma instruments.

The persistence of these wave signatures over hundreds to thousands of Enceladus radii highlights the importance of long-range electrodynamic coupling mediated by Alfvén waves. However, the cadence and coverage of Cassini limited our ability to fully resolve the dynamics of the Enceladus–Saturn interaction. Future missions, therefore, have a crucial role in extending Cassini's legacy. Notably, Enceladus has been selected as the target of the European Space Agency's (ESA) next large-class mission (L4), currently in the planning phase (ESA Expert Committee, 2024). Our findings underscore the importance of equipping such a mission with high-sensitivity electric and magnetic field, particles, and ultraviolet instruments capable of detecting faint Alfvénic perturbations and their various signatures along the field lines connected to Enceladus' plasma torus. Continuous observations near the moon, in the equatorial plane, between 1 R_E and 10 R_E, in its far downstream wake, between 10 R_E and 100 R_E, and at the polar latitudes of the gas giant Saturn, would enable the following: the detection of faint auroral features, detailed characterization of the MAWs, RAWs and their plausible filamentation. Moreover, such a future mission would allow us to better understand the role of the plasma torus in the electrodynamic coupling with Saturn's ionosphere and assess the influence of the plume mass loading and dusty plasma on long-range interaction between Enceladus and its host planet. For instance, an important question that remains open is: are there kilometer-long emissions induced by Enceladus, analogous to the decameter emissions observed for Io, Europa, or Ganymede? These emissions require out-of-equilibrium beams of a few keV. Conversely, there are undoubtedly many more frequent auroral hiss events that can be generated by less energetic electron beams (a few 10–100 eV).

5. Summary and Conclusions

This study presents in situ evidence of an extended and complex electrodynamic coupling between Enceladus and Saturn, based on magnetic and electric field measurements and particle data from the Cassini mission. We identify 36 events with clear Alfvénic signatures, including 13 newly reported cases from non-flyby paths. The main results obtained from their analysis can be summarized as follows:

1. *Large-scale perturbations*: Both the main Alfvén wing and the reflected Alfvén wings (at Saturn's ionosphere and/or along the density gradient of the moon's plasma torus) can be observed distinctly depending on the distance from the moon.

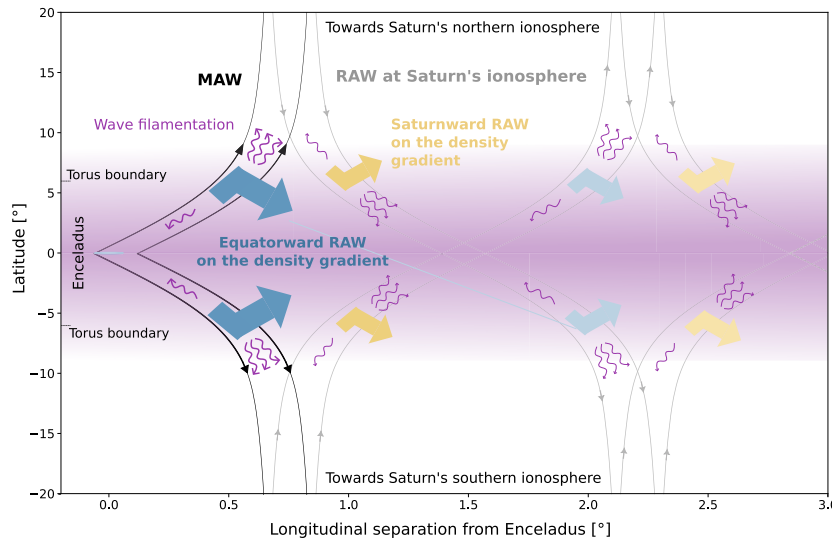

Figure 7. Sketch summarizing our interpretation of the Enceladus-Saturn Alfvén wing system using the same MAWs and RAWs model lines as in Figure 6. For clarity, the downstream extension has been limited to two reflection structures.

2. *Small-scale perturbations*: A systematic filamentation associated with these large-scale perturbations is detected (see Figure 7).
3. *Spatial extent*: Enceladus' interaction region inferred from these wave features extends at least ∼120° $\left(\sim 2000\, R_E\right)$ downstream.
4. *Extended plasma wake*: The occurrence of large-scale perturbations with high power tailward, down to about 2 R_E from the moon's center, suggests the presence of a dense and extended plasma wake that contributes to the MAW generation.
5. *Exponential decay of the large-scale Alfvén wave power*: The overall variation in power downstream between 0° and 60° longitudinal separation from the moon, is well described by an exponential fit spanning about three orders of magnitude. The observed longitudinal e-folding distance is 7.4°, which is consistent with theoretical estimates derived from a multi-reflection model using an energy flux reflection coefficient between 0.8 and 0.9.
6. *North–south asymmetry of the Alfvénic signatures*: The overall MAW generation appears approximately symmetric to first order; however, enhanced small-scale perturbations and stronger filamentation are observed in the southern hemisphere. These features are consistent with additional mass loading and conductivity increases associated with Enceladus' southward water plumes.
7. *Variability*: The electrodynamic coupling displays both a temporal variability, likely related to the dynamic interaction between the plumes, the ionosphere, and the plasma torus, and a spatial variability associated with the patchiness of the RAW regions.
8. *Effects on energetic particle*: In several cases, these wave perturbations are accompanied by energetic electron dropouts, supporting the interpretation that the absorption process of these electrons by the moon leads to a broad and persistent signature on their distribution functions within Enceladus L-shell.

Together, these observations demonstrate that Enceladus' plasma environment and its coupling to Saturn are more extended, structured, and variable than previously recognized. Nevertheless, many questions remain open: the lack of measurements between ∼1 R_E and ∼100 R_E in the equatorial plane prevents detailed analysis of the Alfvén wave reflections within the plasma torus. Moreover, the absence of electron observations for most events farther downstream limits our ability to determine whether TEBs are present in that region or not and if it triggers Alfvénic perturbation within the plasma torus. Our results hence highlight the need for future missions with enhanced sensitivity and sustained measurements in and beyond the moon's extended interaction region. A summary table of the non-flyby events analyzed in this study, including their associated waves and plasma features, is provided to facilitate future comparative and modeling work (Table 1). A summary table of all Enceladus flybys can be found in Saur et al. (2024).

Journal of Geophysical Research: Space Physics
10.1029/2025JA034657

Table 1
Summary of All Non-Flyby Events Exhibiting a Signature of Electrodynamic Interaction Between Enceladus and Saturn

Name	Rev	DOY	Date	Time interval	$\Delta\lambda$ [°]	Θ [°]	Δr [R_E]	<PSD> $[nT^2Hz^{-1}]$	S $[Wm^{-2}]$	Power $[10^9$ W]	Alfvén waves	Pick-up ICW	Electron beam	Energetic e^- dropout	V-shaped auroral hiss
E02	011	195	2005-07-14	22:52:00–22:54:00	13.4	15.9	222	4.4×10^{-2}	5.3×10^{-7}	1.3×10^{-4}	Yes	No	Yes[a]	Yes	No
H	015	266	2005-09-23	18:02:30–18:07:00	56.80	0.06	933	1.4×10^{-2}	9.2×10^{-9}	3.2×10^{-6}	Yes	Yes	Yes[a]	No	No
T37	052	321	2007-11-17	08:40:39–09:01:42	45.2	−3.9	742	4.5×10^{-3}	3.7×10^{-7}	1.3×10^{-4}	Yes	Yes	No	No	No
T37	052	321	2007-11-17	09:17:15–09:20:58	47.1	−4.3	774	2.5×10^{-3}	5.5×10^{-8}	1.8×10^{-5}	Yes	Yes	No	No	No data
—	074	182	2008-06-30	07:26:00–07:29:00	16.1	29.3	273	N/A[b]	N/A[b]	N/A[b]	N/A[b]	N/A[b]	Yes[a]	No	No
—	074	182	2008-06-30	10:05:00–10:06:00	6.2	−32.6	103	N/A[b]	N/A[b]	N/A[b]	N/A[b]	N/A[b]	Yes[a]	No	No
—	087	276	2008-10-02	10:18:58–10:19:34	132.8	7.04	2,186	8.7×10^{-3}	7.4×10^{-7}	2.6×10^{-4}	Yes	Yes	Yes	No	No
T66	125	027	2010-01-27	00:32:32–00:35:17	29.8	−3.6	491	2.1×10^{-3}	1.1×10^{-8}	3.8×10^{-6}	Yes	No	Yes[a]	No	No
T71	134	186	2010-07-05	01:55:00–01:59:58	11.3	−8.8	186	1.4×10^{-2}	2.2×10^{-6}	7.6×10^{-4}	Yes	Yes	Maybe	Yes	No
E11	136	226	2010-08-14	03:53:15–04:01:10	30.0	4.6	496	9.1×10^{-3}	7.2×10^{-8}	2.5×10^{-5}	Yes	No	No	No	No
T78	153	257	2011-09-14	02:11:30–02:17:48	21	−0.37	346	8.0×10^{-2}	4.3×10^{-8}	1.5×10^{-5}	Yes	Yes	No data[c]	Yes	No data
T79	158	346	2011-12-12	05:01:02–05:06:06	5.9	−0.16	97	1.1×10^{-1}	2.0×10^{-6}	6.9×10^{-4}	Yes	Yes	No data[c]	Yes	No data
T82	161	052	2012-02-21	02:15:06–02:18:54	11	−0.06	190	9.2×10^{-2}	2.8×10^{-7}	9.8×10^{-5}	Yes	Yes	No data[c]	Yes	No
—	227	340	2015-12-06	16:36:30–16:41:00	33.7	1.31	556	3.4×10^{-2}	3.5×10^{-8}	1.2×10^{-5}	Yes	Yes	No data[c]	No	No data
115	230	014	2016-01-14	03:08:39–03:12:08	17.7	1.29	291	1.6×10^{-1}	2.0×10^{-7}	7.0×10^{-5}	Yes	Yes	No data[c]	No	No
—	250	332	2016-11-27	06:00:39–06:05:00	359.9	11.9	−1.79	N/A[d]	N/A[d]	N/A[d]	No	No	No data[c]	No	Yes[e]
GF21	291	245	2017-09-02	12:20:52–12:21:54	4.2	52.4	70	2.4×10^{-1}	6.6×10^{-4}	7.2×10^{-3}	Yes	No	No data[c]	No	Yes[e]

[a]See Supporting Information S1 and Rabia et al. (2025). [b]MAG data are noisy. [c]CAPS is not operational. [d]Upstream high latitude event (see main text). [e]See Sulaiman et al. (2018).

Conflict of Interest

The authors declare no conflicts of interest relevant to this study.

Data Availability Statement

All the data used in this project are available on NASA's Planetary Data System/Planetary Plasma Interactions (PSD/PPI) website (https://pds-ppi.igpp.ucla.edu/) and the APIS data service (https://apis.obspm.fr) for Cassini/UVIS data and the french Centre de Données de Physique des Plasmas (CDPP) using Amda tool (https://amda.irap.omp.eu/). The data analysis has been done using Python and loading the data from Amda was done using Speasy is a free and open-source Python package (Jeandet & Schulz, 2025). Events selection was initially done using SciQLop (SCIentific Qt application for Learning from Observations of Plasmas), a user-friendly open source tool designed for the visualization and analysis of in situ space plasma data (https://github.com/SciQLop/SciQLop).

Acknowledgments
The french co-authors acknowledge support from CNES and CNRS/INSU national programs of planetology (PNP) and of solar-terrestrial interactions (ATST, also funded by CEA). L.Z.H. acknowledges the contributions of intern students, Nicolas Halley and Arthur Paradis, to this project. A.J.C. and G.H.J. acknowledge partial support by the UK Science and Technology Facilities Council through consolidated Grant ST/W001004/1. The work of MKGH was supported by the Research Ireland Pathway Programme (Grant 22/PATH-S/10757). The CDPP/AMDA tool received support through the VESPA and SPIDER activities of Europlanet 2024RI funded by the European Union's Horizon 2020 research and innovation programme under Grant Agreement No. 871149.

References

Andriopoulou, M., Roussos, E., Krupp, N., Paranicas, C., Thomsen, M., Krimigis, S., et al. (2014). Spatial and temporal dependence of the convective electric field in Saturn's inner magnetosphere. *Icarus*, *229*, 57–70. https://doi.org/10.1016/j.icarus.2013.10.028

Belcher, J. W., Goertz, C. K., Sullivan, J. D., & Acuña, M. H. (1981). Plasma observations of the alfvén wave generated by Io. *Journal of Geophysical Research*, *86*(A10), 8508–8512. https://doi.org/10.1029/JA086iA10p08508

Bigg, E. K. (1964). Influence of the satellite Io on Jupiter's decametric emission. *Nature*, *203*(4949), 1008–1010. https://doi.org/10.1038/2031008a0

Bonfond, B., Gladstone, G. R., Grodent, D., Greathouse, T. K., Versteeg, M. H., Hue, V., et al. (2017). Morphology of the UV aurorae Jupiter during juno's first perijove observations. *Geophysical Research Letters*, *44*(10), 4463–4471. https://doi.org/10.1002/2017GL073114

Bonfond, B., Grodent, D., Badman, S., Saur, J., Gérard, J.-C., & Radioti, A. (2017). Similarity of the Jovian satellite footprints: Spots multiplicity and dynamics. *Icarus*, *292*, 208–217. https://doi.org/10.1016/j.icarus.2017.01.009

Bonfond, B., Grodent, D., Gérard, J.-C., Radioti, A., Dols, V., Delamere, P. A., & Clarke, J. T. (2009). The Io UV footprint: Location, inter-spot distances and tail vertical extent. *Journal of Geophysical Research*, *114*(A7), A07224. https://doi.org/10.1029/2009JA014312

Bonfond, B., Grodent, D., Gérard, J.-C., Radioti, A., Saur, J., & Jacobsen, S. (2008). UV Io footprint leading spot: A key feature for understanding the uv io footprint multiplicity? *Geophysical Research Letters*, *35*(5), L05107. https://doi.org/10.1029/2007GL032418

Bonfond, B., Saur, J., Grodent, D., Badman, S. V., Bisikalo, D., Shematovich, V., et al. (2017). The tails of the satellite Auroral footprints at Jupiter. *Journal of Geophysical Research: Space Physics*, *122*(8), 7985–7996. https://doi.org/10.1002/2017JA024370

Bonfond, B., & Sulaiman, A. (2024). Alfvén waves related to moon–magnetosphere interactions. In *Alfvén waves across heliophysics* (pp. 139–161). American Geophysical Union (AGU). https://doi.org/10.1002/9781394195985.ch7

Chust, T., Roux, A., Kurth, W., Gurnett, D., Kivelson, M., & Khurana, K. (2005). Are io's alfvén wings filamented? Galileo observations. *Planetary and Space Science*, *53*(4), 395–412. https://doi.org/10.1016/j.pss.2004.09.021

Clarke, J. T., Ajello, J., Ballester, G., Ben Jaffel, L., Connerney, J., Gérard, J.-C., et al. (2002). Ultraviolet emissions from the magnetic footprints of io, ganymede and europa on Jupiter. *Nature*, *415*(6875), 997–1000. https://doi.org/10.1038/415997a

Clarke, J. T., Ballester, G. E., Trauger, J., Evans, R., Connerney, J. E. P., Stapelfeldt, K., et al. (1996). Far-ultraviolet imaging of jupiter's Aurora and the io "footprint". *Science*, *274*(5286), 404–409. https://doi.org/10.1126/science.274.5286.404

Connerney, J. E. P., Baron, R., Satoh, T., & Owen, T. (1993). Images of excited H_3^+ at the foot of the io flux tube in jupiter's atmosphere. *Science*, *262*(5136), 1035–1038. https://doi.org/10.1126/science.262.5136.1035

Dougherty, M. K., Cao, H., Khurana, K. K., Hunt, G. J., Provan, G., Kellock, S., et al. (2018). Saturn's magnetic field revealed by the cassini grand finale. *Science*, *362*(6410), eaat5434. https://doi.org/10.1126/science.aat5434

Dougherty, M. K., Kellock, S., Southwood, D. J., Balogh, A., Smith, E. J., Tsurutani, B. T., et al. (2004). The Cassini magnetic field investigation. *Space Science Reviews*, *114*(1), 331–383. https://doi.org/10.1007/s11214-004-1432-2

Dougherty, M. K., Khurana, K. K., Neubauer, F. M., Russell, C. T., Saur, J., Leisner, J. S., & Burton, M. E. (2006). Identification of a dynamic atmosphere at Enceladus with the Cassini magnetometer. *Science*, *311*(5766), 1406–1409. https://doi.org/10.1126/science.1120985

Drell, S. D., Foley, H. M., & Ruderman, M. A. (1965). Drag and propulsion of large satellites in the ionosphere: An alfvén propulsion engine in space. *Journal of Geophysical Research*, *70*(13), 3131–3145. https://doi.org/10.1029/JZ070i013p03131

Engelhardt, I., Wahlund, J.-E., Andrews, D., Eriksson, A., Ye, S., Kurth, W., et al. (2015). Plasma regions, charged dust and field-aligned currents near enceladus. *Planetary and Space Science*, *117*, 453–469. https://doi.org/10.1016/j.pss.2015.09.010

ESA Expert Committee. (2024). *Report of the expert committee for the large-class mission in ESA's voyage 2050 plan covering the science theme "Moons of the Giant Planets" (L4 final report)*. European Space Agency. Retrieved from https://www.cosmos.esa.int/documents/1866264/1866292/ESA_L4_Expert_Committee_report_Voyage_2050_Moons_of_the_Giant_Planets.pdf

Gérard, J.-C., Saglam, A., Grodent, D., & Clarke, J. T. (2006). Morphology of the ultraviolet io footprint emission and its control by io's location. *Journal of Geophysical Research*, *111*(A4), A04202. https://doi.org/10.1029/2005JA011327

Gershman, D. J., Connerney, J. E. P., Kotsiaros, S., DiBraccio, G. A., Martos, Y. M., Viñas, A. F., et al. (2019). Alfvénic fluctuations associated with jupiter's auroral emissions. *Geophysical Research Letters*, *46*(13), 7157–7165. https://doi.org/10.1029/2019GL082951

Gurnett, D. A., Averkamp, T. F., Schippers, P., Persoon, A. M., Hospodarsky, G. B., Leisner, J. S., et al. (2011). Auroral hiss, electron beams and standing alfvén wave currents near saturn's moon enceladus. *Geophysical Research Letters*, *38*(6), L06102. https://doi.org/10.1029/2011GL046854

Gurnett, D. A., Kurth, W. S., Kirchner, D. L., Hospodarsky, G. B., Averkamp, T. F., Zarka, P., et al. (2004). The Cassini radio and plasma wave investigation. *Space Science Reviews*, *114*(1–4), 395–463. https://doi.org/10.1007/s11214-004-1434-0

Hess, S., Delamere, P., Dols, V., Bonfond, B., & Swift, D. (2010). Power transmission and particle acceleration along the io flux tube. *Journal of Geophysical Research*, *115*(A6), A06205. https://doi.org/10.1029/2009JA014928

Hess, S., Delamere, P. A., Dols, V., & Ray, L. C. (2011). Comparative study of the power transferred from satellite-magnetosphere interactions to auroral emissions. *Journal of Geophysical Research*, *116*(A1), A01202. https://doi.org/10.1029/2010JA015807

Hess, S., Mottez, F., & Zarka, P. (2007). Jovian s burst generation by alfvén waves. *Journal of Geophysical Research*, *112*(A11), A11212. https://doi.org/10.1029/2006JA012191

Hinton, P. C., Bagenal, F., & Bonfond, B. (2019). Alfvén wave propagation in the io plasma torus. *Geophysical Research Letters*, *46*(3), 1242–1249. https://doi.org/10.1029/2018GL081472

Hue, V., Gladstone, G. R., Louis, C. K., Greathouse, T. K., Bonfond, B., Szalay, J. R., et al. (2023). The io, europa, and ganymede auroral footprints at Jupiter in the ultraviolet: Positions and equatorial lead angles. *Journal of Geophysical Research: Space Physics*, *128*(5), e2023JA031363. https://doi.org/10.1029/2023JA031363

Jeandet, A., & Schulz, A. (2025). Speasy. https://doi.org/10.5281/zenodo.15583262

Jia, Y.-D., Russell, C. T., Khurana, K. K., Wei, H. Y., Ma, Y. J., Leisner, J. S., et al. (2011). Cassini magnetometer observations over the enceladus poles. *Geophysical Research Letters*, *38*(19), L19109. https://doi.org/10.1029/2011GL049013

Jones, G. H., Roussos, E., Krupp, N., Paranicas, C., Woch, J., Lagg, A., et al. (2006). Enceladus' varying imprint on the magnetosphere of Saturn. *Science*, *311*(5766), 1412–1415. https://doi.org/10.1126/science.1121011

Khurana, K. K., Kivelson, M. G., Stevenson, D. J., Schubert, G., Russell, C. T., Walker, R. J., & Polanskey, C. (1998). Induced magnetic fields as evidence for subsurface oceans in europa and callisto. *Nature*, *395*(6704), 777–780. https://doi.org/10.1038/27394

Kim, K., Edberg, N. J. T., Wahlund, J.-E., & Vigren, E. (2024). Alfvén wing-like structures in titan's magnetotail during t122-t126 flybys. *Journal of Geophysical Research: Space Physics*, *129*(6), e2023JA032265. https://doi.org/10.1029/2023JA032265

Kivelson, M. G., Khurana, K. K., Stevenson, D. J., Bennett, L., Joy, S., Russell, C. T., et al. (1999). Europa and callisto: Induced or intrinsic fields in a periodically varying plasma environment. *Journal of Geophysical Research*, *104*(A3), 4609–4625. https://doi.org/10.1029/1998JA900095

Kivelson, M. G., Khurana, K. K., Walker, R. J., Russell, C. T., Linker, J. A., Southwood, D. J., & Polanskey, C. (1996). A magnetic signature at io: Initial report from the galileo magnetometer. *Science*, *273*(5273), 337–340. https://doi.org/10.1126/science.273.5273.337

Kriegel, H., Simon, S., Motschmann, U., Saur, J., Neubauer, F. M., Persoon, A. M., et al. (2011). Influence of negatively charged plume grains on the structure of enceladus' alfvén wings: Hybrid simulations versus cassini magnetometer data. *Journal of Geophysical Research*, *116*(A10), A10223. https://doi.org/10.1029/2011JA016842

Krimigis, S. M., Mitchell, D. G., Hamilton, D. C., Livi, S., Dandouras, J., Jaskulek, S., et al. (2004). Magnetosphere imaging instrument (mimi) on the cassini mission to Saturn/Titan. *Space Science Reviews*, *114*(1), 233–329. https://doi.org/10.1007/s11214-004-1410-8

Leisner, J. S., Hospodarsky, G. B., & Gurnett, D. A. (2013). Enceladus auroral hiss observations: Implications for electron beam locations. *Journal of Geophysical Research: Space Physics*, *118*(1), 160–166. https://doi.org/10.1029/2012JA018213

Leisner, J. S., Russell, C. T., Dougherty, M. K., Blanco-Cano, X., Strangeway, R. J., & Bertucci, C. (2006). Ion cyclotron waves in saturn's e ring: Initial cassini observations. *Geophysical Research Letters*, *33*(11), L11101. https://doi.org/10.1029/2005GL024875

Louis, C. K., Lamy, L., Zarka, P., Cecconi, B., & Hess, S. L. G. (2017). Detection of Jupiter decametric emissions controlled by europa and ganymede with voyager/pra and cassini/rpws. *Journal of Geophysical Research: Space Physics*, *122*(9), 9228–9247. https://doi.org/10.1002/2016JA023779

Louis, C. K., Louarn, P., Collet, B., Clément, N., Al Saati, S., Szalay, J. R., et al. (2023). Source of radio emissions induced by the Galilean moons Io, Europa and Ganymede: In situ measurements by Juno. *Journal of Geophysical Research: Space Physics*, *128*(12), e2023JA031985. https://doi.org/10.1029/2023JA031985

Neubauer, F. (1980). Nonlinear standing alfvén wave current system at io: Theory. *Journal of Geophysical Research*, *85*(A3), 1171–1178. https://doi.org/10.1029/JA085iA03p01171

Persoon, A. M., Kurth, W. S., Gurnett, D. A., Faden, J. B., Groene, J. B., Morooka, M. W., et al. (2020). Distribution in saturn's inner magnetosphere from 2.4 to 10 rs: A diffusive equilibrium model. *Journal of Geophysical Research: Space Physics*, *125*(3), e2019JA027545. https://doi.org/10.1029/2019JA027545

Porco, C. C., Helfenstein, P., Thomas, P. C., Ingersoll, A. P., Wisdom, J., West, R., et al. (2006). Cassini observes the active south pole of enceladus. *Science*, *311*(5766), 1393–1401. https://doi.org/10.1126/science.1123013

Prangé, R., Rego, D., Southwood, D., Zarka, P., Miller, S., & Ip, W. (1996). Correction: Rapid energy dissipation and variability of the lo-Jupiter electrodynamic circuit. *Nature*, *380*(6573), 460. https://doi.org/10.1038/380460a0

Pryor, W. R., Magalhães, F. P., Lamy, L., Prangé, R., Esposito, L. W., Gustin, J., et al. (2024). Cassini uvis observations of the enceladus auroral footprint on Saturn in 2017. *The Planetary Science Journal*, *5*(1), 20. https://doi.org/10.3847/PSJ/ad0cbc

Pryor, W. R., Rymer, A. M., Mitchell, D. G., Hill, T. W., Young, D. T., Saur, J., et al. (2011). The auroral footprint of Enceladus on Saturn. *Nature*, *472*(7343), 331–333. https://doi.org/10.1038/nature09928

Rabia, J., Hadid, L., André, N., Nénon, Q., Chust, T., Pisa, D., et al. (2025). Cassini caps-els observations of low-energy electron beams within enceladus mid-latitude flux tubes. *Geophysical Research Letters*, *52*(22), e2025GL119448. https://doi.org/10.1029/2025GL119448

Rabia, J., Hue, V., André, N., Nénon, Q., Szalay, J. R., Allegrini, F., et al. (2024). Properties of electrons accelerated by the ganymede-magnetosphere interaction: Survey of juno high-latitude observations. *Journal of Geophysical Research: Space Physics*, *129*(5), e2024JA032604. https://doi.org/10.1029/2024JA032604

Roussos, E., Jones, G. H., Krupp, N., Paranicas, C., Mitchell, D. G., Lagg, A., et al. (2007). Electron microdiffusion in the saturnian radiation belts: Cassini mimi/lemms observations of energetic electron absorption by the icy moons. *Journal of Geophysical Research*, *112*(A6), A06214. https://doi.org/10.1029/2006JA012027

Roussos, E., Krupp, N., Woch, J., Lagg, A., Jones, G. H., Paranicas, C., et al. (2005). Low energy electron microsignatures at the orbit of tethys: Cassini mimi/lemms observations. *Geophysical Research Letters*, *32*(24), L24107. https://doi.org/10.1029/2005GL024084

Saur, J. (2004). A model of io's local electric field for a combined alfvénic and unipolar inductor far-field coupling. *Journal of Geophysical Research*, *109*(A1), A01210. https://doi.org/10.1029/2002JA009354

Saur, J. (2021). Overview of moon–magnetosphere interactions. In *Magnetospheres in the solar system* (pp. 575–593). American Geophysical Union (AGU). https://doi.org/10.1002/9781119815624.ch36

Saur, J., Duling, S., Grayver, A., & Szalay, J. R. (2024). Analysis of enceladus's time-variable space environment to magnetically sound its interior. *The Planetary Science Journal*, *5*(11), 245. https://doi.org/10.3847/PSJ/ad8130

Saur, J., Grambusch, T., Duling, S., Neubauer, F. M., & Simon, S. (2013). Magnetic energy fluxes in sub-alfvénic planet star and moon planet interactions. *A&A*, *552*, A119. https://doi.org/10.1051/0004-6361/201118179

Saur, J., Neubauer, F. M., & Schilling, N. (2007). Hemisphere coupling in enceladus' asymmetric plasma interaction. *Journal of Geophysical Research*, *112*(A11), A11209. https://doi.org/10.1029/2007JA012479

Simon, S., Saur, J., Kriegel, H., Neubauer, F. M., Motschmann, U., & Dougherty, M. K. (2011). Influence of negatively charged plume grains and hemisphere coupling currents on the structure of enceladus' alfvén wings: Analytical modeling of cassini magnetometer observations. *Journal of Geophysical Research*, *116*(A4), A04221. https://doi.org/10.1029/2010JA016338

Sulaiman, A. H., Kurth, W. S., Connerney, J. E. P., Elliott, S. S., Hospodarsky, G. B., Kruegler, N. S., et al. (2024). Io's near-field Alfven wings and local electron beams inferred from juno/waves. *Geophysical Research Letters*, *51*(15), e2024GL110206. https://doi.org/10.1029/2024GL110206

Sulaiman, A. H., Kurth, W. S., Hospodarsky, G. B., Averkamp, T. F., Ye, S.-Y., Menietti, J. D., et al. (2018). Enceladus auroral hiss emissions during cassini's grand finale. *Geophysical Research Letters*, *45*(15), 7347–7353. https://doi.org/10.1029/2018GL078130

Sulaiman, A. H., Szalay, J. R., Clark, G., Allegrini, F., Bagenal, F., Brennan, M. J., et al. (2023). Poynting fluxes, field-aligned current densities, and the efficiency of the io-jupiter electrodynamic interaction. *Geophysical Research Letters*, *50*(10), e2023GL103456. https://doi.org/10.1029/2023GL103456

Szalay, J. R., Allegrini, F., Bagenal, F., Bolton, S. J., Bonfond, B., Clark, G., et al. (2020). A new framework to explain changes in io's footprint tail electron fluxes. *Geophysical Research Letters*, *47*(18), e2020GL089267. https://doi.org/10.1029/2020GL089267

Szalay, J. R., Bonfond, B., Allegrini, F., Bagenal, F., Bolton, S., Clark, G., et al. (2018). In situ observations connected to the io footprint tail Aurora. *Journal of Geophysical Research: Planets*, *123*(11), 3061–3077. https://doi.org/10.1029/2018JE005752

Tokar, R. L., Johnson, R. E., Hill, T. W., Pontius, D. H., Kurth, W. S., Crary, F. J., et al. (2006). The interaction of the atmosphere of enceladus with saturn's plasma. *Science*, *311*(5766), 1409–1412. https://doi.org/10.1126/science.1121061

Tokar, R. L., Johnson, R. E., Thomsen, M. F., Wilson, R. J., Young, D. T., Crary, F. J., et al. (2009). Cassini detection of enceladus' cold water-group plume ionosphere. *Geophysical Research Letters*, *36*(13), L13203. https://doi.org/10.1029/2009GL038923

Wright, A. N., & Schwartz, S. J. (1989). The transmission of alfven waves through the io plasma torus. *Journal of Geophysical Research*, *94*(A4), 3749–3754. https://doi.org/10.1029/JA094iA04p03749

Young, D. T., Berthelier, J. J., Blanc, M., Burch, J. L., Coates, A. J., Goldstein, R., et al. (2004). Cassini plasma spectrometer investigation. *Space Science Reviews*, *114*, 1–112. https://doi.org/10.1007/978-1-4020-2774-1_1

Zarka, P. (1998). Auroral radio emissions at the outer planets: Observations and theories. *Journal of Geophysical Research*, *103*(E9), 20159–20194. https://doi.org/10.1029/98JE01323

Zarka, P., Marques, M. S., Louis, C., Ryabov, V. B., Lamy, L., Echer, E., & Cecconi, B. (2018). Jupiter radio emission induced by ganymede and consequences for the radio detection of exoplanets. *A&A*, *618*, A84. https://doi.org/10.1051/0004-6361/201833586